

Article

## Semantic Decomposition and Reconstruction of Compound Buildings with Symmetric Roofs from LiDAR Data and Aerial Imagery

Hongtao Wang <sup>1,2</sup>, Wuming Zhang <sup>1,\*</sup>, Yiming Chen <sup>1</sup>, Mei Chen <sup>1</sup> and Kai Yan <sup>1</sup>

<sup>1</sup> State Key Laboratory of Remote Sensing Science, Beijing Key Laboratory of Environmental Remote Sensing and Digital City, School of Geography, Beijing Normal University, Beijing 100875, China; E-Mails: wht\_31@hpu.edu.cn (H.W.); cym\_bnu@mail.bnu.edu.cn (Y.C.); 627cm@tongji.edu.cn (M.C.); kyan@mail.bnu.edu.cn (K.Y.)

<sup>2</sup> School of Surveying and Land Information Engineering, Henan Polytechnic University, Jiaozuo 454003, China

\* Author to whom correspondence should be addressed; E-Mail: wumingz@bnu.edu.cn; Tel./Fax: +86-10-5880-9246.

Academic Editors: Norman Kerle and Prasad S. Thenkabail

Received: 11 August 2015 / Accepted: 19 October 2015 / Published: 23 October 2015

---

**Abstract:** 3D building models are important for many applications related to human activities in urban environments. However, due to the high complexity of the building structures, it is still difficult to automatically reconstruct building models with accurate geometric description and semantic information. To simplify this problem, this article proposes a novel approach to automatically decompose the compound buildings with symmetric roofs into semantic primitives by exploiting local symmetry contained in the building structure. In this approach, the proposed decomposition allows the overlapping of neighbor primitives and each decomposed primitive can be represented as a parametric form, which simplify the complexity of the building reconstruction and facilitate the integration of LiDAR data and aerial imagery into a parameters optimization process. The proposed method starts by extracting isolated building regions from the LiDAR point clouds. Next, point clouds belonging to each compound building are segmented into planar patches to construct an attributed graph, and then the local symmetries contained in the attributed graph are exploited to automatically decompose the compound buildings into different semantic primitives. In the final step, 2D image features are extracted depending on the initial 3D primitives generated from LiDAR data, and then the compound building

is reconstructed using constraints from LiDAR data and aerial imagery by a nonlinear least squares optimization. The proposed method is applied to two datasets with different point densities to show that the complexity of building reconstruction can be reduced considerably by decomposing the compound buildings into semantic primitives. The experimental results also demonstrate that the traditional model driven methods can be further extended to the automated reconstruction of compound buildings by using the proposed semantic decomposition method.

**Keywords:** semantic decomposition; compound building modeling; LiDAR point cloud; aerial imagery; attributed graph

---

## 1. Introduction

3D building models are the most prominent features in digital cities and have many applications in geographic information systems, urban planning, disaster management, emergency response, virtual tourism, and so on. Due to the current rapid development of cities and the requirement for up-to-date information, the automatic reconstruction of 3D building models has been an active research field in photogrammetry and computer vision, and many approaches have been proposed on this topic based on either photogrammetric data or LiDAR data. However, the reliable and automatic generation of detailed large-scale building models is still a difficult and time-consuming task. In particular, the automated generation of 3D building models with complex structures still remains a challenging issue [1,2].

Two fundamentally different methods have been used for automated 3D building reconstruction: data-driven methods and model-driven methods. For data-driven methods, a common assumption is that buildings have a polyhedral form, *i.e.*, buildings only have planar roofs. Therefore, these methods usually start with the extraction of planar patches from LiDAR point clouds using segmentation algorithms, such as region growing [3], random sample consensus [4], 3D Hough transform [5], and clustering methods [6,7]. Based on this segmentation, polyhedral building models are then generated from these planar patches by intersection and step edge generation, and then some regularization rules are often used to improve the shape of the reconstructed building model [7–9]. The main advantage of the data-driven approach is that it can reconstruct polyhedral buildings with complex shapes. While the main drawback of these methods is their sensitivity to the incompleteness of data arising from occlusion, shadow and/or missing information in the input data. That is, if there are missing features in the data, the modeling process may be hampered and the corresponding object structure may be visually deformed. In this case, aerial imagery can serve as a complementary data source to accurately generate building models due to its high resolution. Thus, a variety of methods using both LiDAR data and optical imagery for building reconstruction have been proposed in the last ten years [10–19]. Among these methods, line segments, and planar patches are mainly used as the basic primitives and the topological relationships are exploited to generate approximate building models, which are then refined using optical images. In this process, most of the aforementioned methods need to search line cues on multi-view aerial images, and then these 2D line segments are matched to derive the accurate 3D building structure. Although image-based edge detection algorithms perform well, matching

ambiguities in multiple images are the main obstacle. Another limitation of the data driven methods is that the models generated from line segments and planar patches are only geometric models, and the semantic information about the buildings' structures is always missed.

To obtain visual impressions and topologically-correct building models with semantic information, geometric constraints, such as parallel and perpendicular lines should be encoded in the building reconstruction [20,21]. Such regularization can be met easily if model driven methods are utilized. The model-driven strategy starts with a hypothetical building model, which is then verified by the consistency of the model with the LiDAR point clouds [22–26] or aerial imagery [27,28]. Recently, the Reversible Jump Markov Chain Monte Carlo (RJMCMC) method has been used to generate the building models [29,30], which performs well in the reconstruction of 3D building models. However, its main limitation is its computational intensity. The advantage of model-driven methods is that they can create compact, watertight, geometric building models with semantic labeling, but their main limitation is that they can only generate certain types of predefined building models in the library, so many existing model-driven methods usually focus on relatively simple buildings [23,27,31].

To reconstruct complex building models by using model-driven method, Constructive Solid Geometry (CSG)-based methods have been proposed by some researchers [5,21,24,26,28,32,33]. Within these approaches, a complex building model is often regarded as a combination of simple roof shapes, and these simple primitives are grouped into complete building models by means of Boolean set operators (union, intersection, and subtraction). Thus, complex buildings can be reconstructed by aggregating the basic building primitives in the library. CSG primitives have semantic information about the model's type and can be represented by a few shape parameters and pose parameters, which are suitable for the building reconstruction. However, automatic decomposition of complex buildings into CSG primitives is difficult, so the CSG modeling methods are usually adopted in a semi-automatic way [27,34,35]. The complexity of this decomposition task has led many studies to use external information, mostly in the form of ground plans or building footprints [5,24,25,28,32,36,37]. Among these methods, 2D maps are used to decompose the compound buildings into non-overlapping building regions, and then the parameters of the parametric model in each building polygon are determined using LiDAR data or aerial imagery. The use of building footprints can simplify the reconstruction of the complex buildings, but it is not always available and often outdated. For the automatic reconstruction of complex buildings without ground plans, some researchers have constructed roof topology graph (a graph indicates the topology relationship between the rooftop planar patches) to interpret the building structures and automatically decompose complex buildings into basic primitives from LiDAR point clouds [12,22,38–40]. By using roof topology graphs, the problem of finding basic shapes in point clouds can be reduced to a sub-graph matching problem, and then the complex scene can be decomposed into some predefined primitives and reconstructed by assembling these basic primitives. However, the decomposition results of these methods are not semantic building primitives, but the combination of planar patches or a set of polygons, which is difficult for architects to interpret and edit. In this paper, the semantic building primitives are defined as object-based parametric building models that hold both geometric and semantic information, which can be easily modified and reproduced.

In reality, complex buildings are often represented as compound buildings, which are the combination of basic primitives. By decomposing the compound buildings into several semantic primitives, the difficulty of building reconstruction can be considerably reduced. To this aim, a

semantic decomposition method is proposed in this paper by exploiting knowledge about local symmetries that are implicitly contained in the building structures. As a result, the compound buildings can be decomposed into some parametric primitives (e.g., gabled roof, half-hipped roof, and hipped roof). Then, each parametric primitive is reconstructed by a primitive-based building modeling method proposed by Zhang *et al.* [41], which was developed to generate basic building primitives using constraints from LiDAR data and aerial imagery. In contrast to the aforementioned reconstruction methods using roof topology graph, the main contribution of this paper can be summarized as follows: (1) automatic decomposition of compound buildings into semantic primitives by using an attributed graph. Different from the aforementioned decomposition methods using roof topology graph, the outputs of the proposed decomposition are semantic primitives which can be represented as fixed parametric forms. Benefiting from this decomposition, the model driven methods can be further extended to the automated reconstruction of the compound buildings; (2) Flexible reconstruction by allowing the overlapping of neighbor primitives. In the process of compound building's decomposition and model recognition, the proposed method allows the overlapping of neighbor primitives, which can considerably simplify the complexity of the building reconstruction because the intersection of neighbor primitives do not need to be defined and only a small set of basic building primitives are contained in the predefined library.

The remainder of this paper is organized as follows. The overview of the proposed method and a detailed description of the proposed semantic decomposition and reconstruction method are given in Section 2. In Section 3, the data sets used in this research are described, and then some experimental results are presented. Some discussions of the proposed method are provided in Section 4. Finally, Section 5 gives this paper's conclusions.

## 2. Methodology

### 2.1. Overview of the Proposed Method

The proposed approach relies on the assumption that most compound buildings can be constructed as a combination of parametric primitives, which have semantic information about the buildings' structures (e.g., gabled roof, half-hipped roof, hipped roof, *etc.*). Based on this knowledge, an automatic decomposition algorithm is proposed to decompose the compound buildings into basic primitives, and then each primitive is reconstructed using constraints from LiDAR data and aerial imagery.

Figure 1 shows the flowchart of the proposed decomposition and reconstruction method, which consists of three main steps. First, isolated building regions are detected and extracted from LiDAR data during data preprocessing. In the second step, point cloud belonging to a compound building roof is segmented into planar patches, and then an attributed graph is constructed among these segmented planar patches. By exploiting knowledge about the local symmetries contained in the attributed graph, the compound buildings are automatically decomposed into semantic building parts. After that, models in each decomposition cell are recognized and estimated. In the final step, 2D corners are efficiently extracted from the aerial imagery depending on the initial models generated from above step, and then each primitive is reconstructed using constraints from LiDAR data and aerial imagery by a nonlinear least squares optimization.

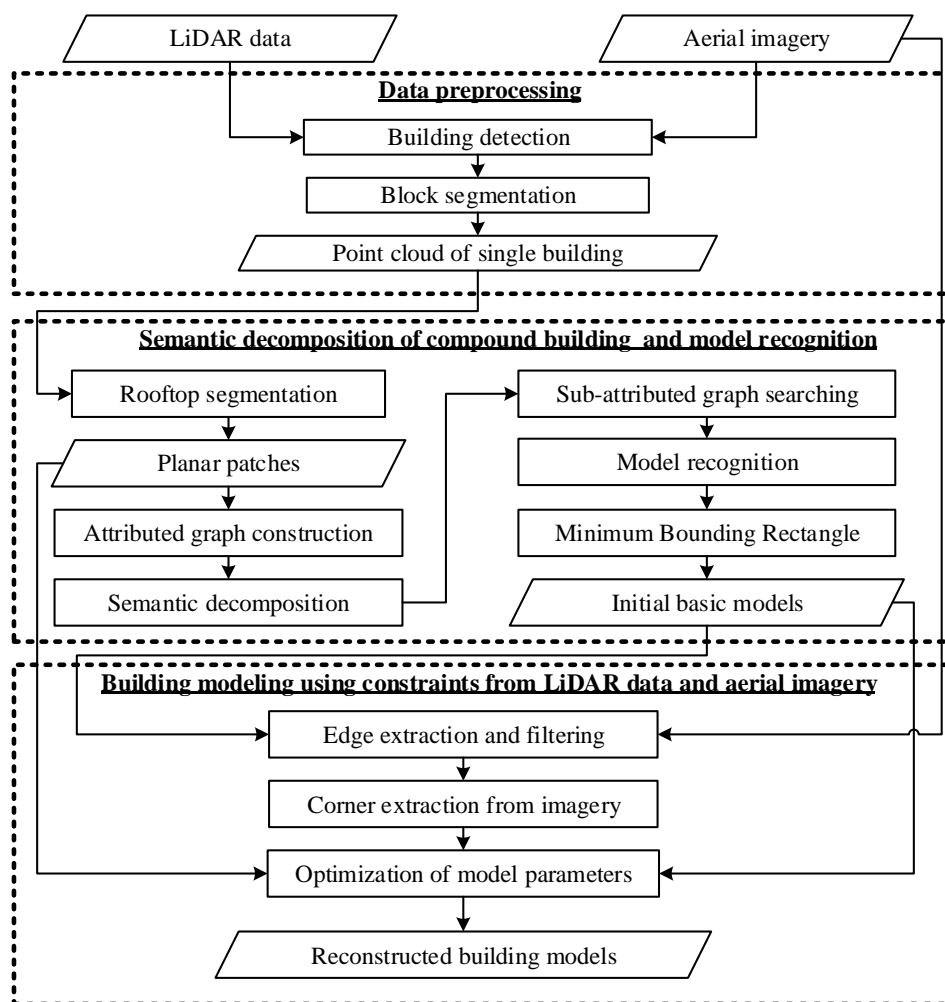


**Figure 1.** Flowchart of the proposed compound building decomposition and reconstruction method.

### 2.2. Data Preprocessing

In this paper, the LiDAR point cloud and multispectral aerial imagery are jointly used in the process of data preprocessing and building reconstruction. During data preprocessing, regions of building blocks are first detected from LiDAR point clouds. It consists of three main steps. First, terrain points are separated from non-terrain points using a filter method proposed by Axelsson [42], and then high-rise points (mostly including building and vegetation points) can be identified from non-terrain points using a specified height threshold above the ground. In this paper, the height threshold is set to 2 m because buildings in the test area are 2 m higher above the ground. Next, every 3D high-rise point is projected back on the multispectral imagery to derive the corresponding Normalized Difference Vegetation Index (NDVI) value, and then most of the tree points can be removed from high-rise points by using an NDVI threshold (0.1 in this paper), which is determined by histogram analysis. Finally, the Euclidean clustering method introduced by Rusu [43] is applied to segment the remaining points into individual clusters, and then the clusters with small area are removed as tree clusters. Note that the area threshold is determined by the point density of the LiDAR point cloud. If the point density of the LiDAR point cloud is 4 points/m<sup>2</sup> (the point density of one data set used in the experiment), clusters with 20 points indicate an area of approximate 5 m<sup>2</sup>. In this case, 20 points are chosen as the threshold

to remove tree clusters smaller than 5 m<sup>2</sup>. After the aforementioned process, building points will be detected and segmented into clusters that represent the individual buildings, and then building models can be subsequently reconstructed from each collection.

### 2.3. Semantic Decomposition of the Compound Building and the Primitive Recognition

By making careful observations from aerial imagery, it can be seen that most compound buildings have multiple ridge lines and each ridge line potentially indicates an individual part of a real building roof. For each ridge line, it is usually constituted by two symmetric planar patches. It is a local symmetry characteristic implicitly contained in the building structure. By exploiting this knowledge about local symmetry, we present an automatic decomposition algorithm to decompose the compound buildings into semantic primitives. Figure 2 illustrates the main framework of this decomposition algorithm, in which a compound building can be decomposed into five primitives using the proposed method.

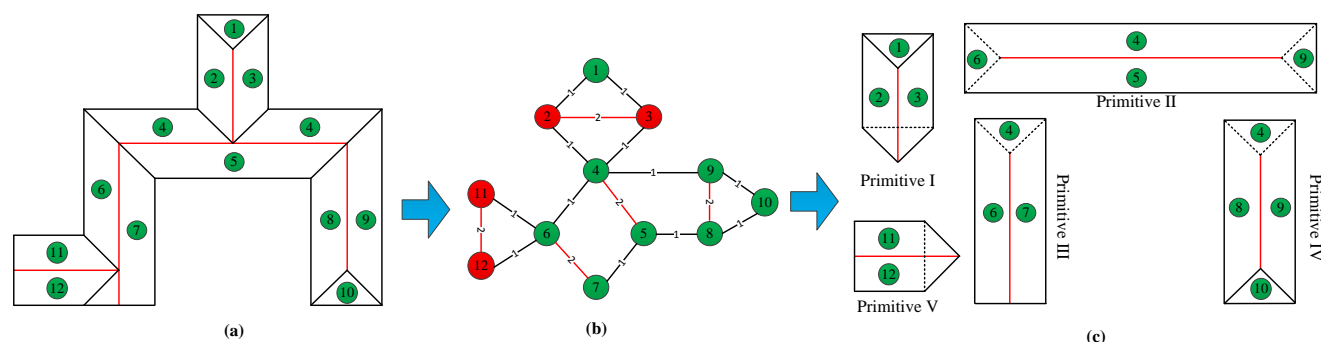


**Figure 2.** Illustration of the proposed semantic decomposition method. (a) A compound building and its segmented planar patches (numbered in green circle); (b) attributed graph of the segmented planar patches; and (c) results of the proposed semantic decomposition.

#### 2.3.1. Construction of the Attributed Graph

The process of automatic decomposition starts with the extraction of planar patches from each building cluster, which was derived from data preprocessing. In this paper, the planar patches are extracted using an adaptive Random Sample Consensus (RANSAC) segmentation algorithm proposed by Chen *et al.* [44], which is suitable for the segmentation of complex rooftops and less sensitive to the uniformity of point clouds. In this algorithm, a local sampling strategy is adopted to select three points from the point cloud for the estimation of a 3D plane model, and then the points within a threshold distance from the estimated model are counted. The process of estimating plane and counting points is repeated for a fixed number of iterations, and then the plane with maximum number of points closer to it is selected as the best candidate. The points that are within the threshold distance to the best candidate are termed as inliers. These points are removed from the complete point dataset, and then RANSAC is again applied on the remaining points to extract remaining dominant planes. This process is repeated until no further planes could be estimated from the remaining points or the remaining points are less than a threshold number. Applying RANSAC iteratively to the point clouds of compound building results in a set of planar patches. Figure 3a shows the segmented planar patches of a compound building, in which each number indicates a segmented planar patch.

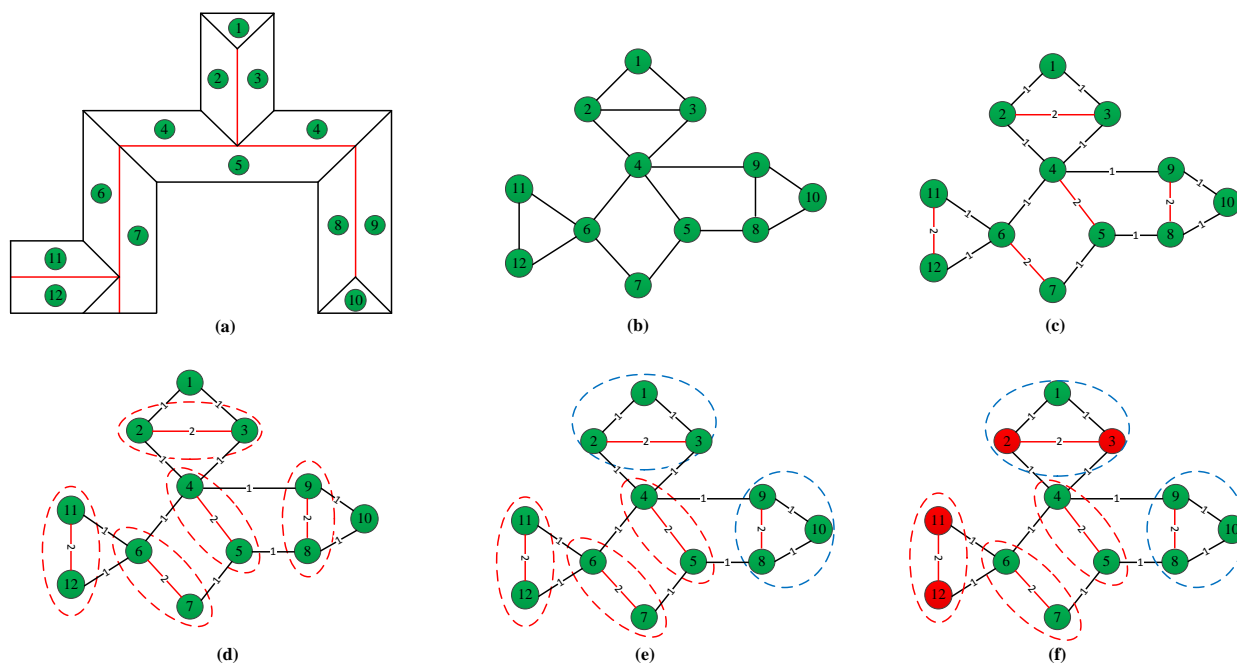


**Figure 3.** The construction of a compound building’s attributed graph. (a) The segmented planar patches of a compound building; (b) adjacency graph of the segmented planar patches; (c) edge labeling according to the normal vector of two adjacent planar patches; (d) extraction of anti-symmetry planar patches; (e) grouping of remaining planar patches; and (f) attributed graph of a compound building.

To decompose the compound buildings into semantic primitives, an adjacency graph is first constructed using the segmented planar segments to encode the building topology. In this graph, each vertex represents a planar patch in the building structure, and an edge between two vertices indicates that the two planar patches are spatially connected. In this study, the adjacency relationships of all pairs of roof planar patches are reconstructed using the boundary points of each planar patch to reduce the complexity of calculation. More specifically, the boundary points of each planar segment are first detected using the alpha shape algorithm [45], and then the distances between two boundary point sets of the planar patches are calculated. The vertices representing two planar patches are connected if two constraints are satisfied: (1) the distance between the boundary point sets of the two planar patches is less than a predefined threshold; and (2) there are sufficient number of corresponding point pairs that satisfy the first constraint. Applying these two criteria, the adjacency relationships of all the pairs of segmented roof planar patches can be determined and used to decompose the compound buildings. Figure 3b shows the adjacency graph of the segmented planar patches shown in Figure 3a.

However, representation solely based on adjacency graphs is not sufficient to discriminate different semantic primitives. To make the decomposition more reliable, another topological relationship is embedded into the adjacency graph, which is the normal direction of each planar segment. Specifically, the topological relationship between two adjacent planar patches can be described by considering the proximity and normal vector of two planar patches. In this paper, the equation of a 3D plane is defined as  $AX + BY + CZ + D = 0$ . In this case, the normal vector of a 3D plane is the plane parameters  $(A, B, C)$ , which can be estimated by a number of 3D points located on the same planar

patches. Then, the angle ( $\theta$ ) between the horizontal components of two normal vectors ( $(A_1, B_1)$  and  $(A_2, B_2)$ ) can be calculated to determine the edge labeling of two vertices (planar patches). If the value of the calculated angle is in the range of  $80^\circ$  to  $100^\circ$ , the horizontal components of these two normal vectors are orthogonal, and the edge between the corresponding vertices (planar patches) is labeled as “1”; if the value of the calculated angle is in the range of  $170^\circ$  to  $180^\circ$ , the horizontal components of these two normal vectors are opposite, and the edge between the corresponding vertices (planar patches) is labeled as “2”. The edge labeling results of the adjacency graph are shown in Figure 3c.

In addition, the attribute of each vertex is also embedded into the adjacency graph to facilitate the semantic decomposition. In this paper, the attribute of each vertex is labeled as “T” or “F”. Vertices labeled as “T” mean that they belong to the attached part of the main building. Otherwise, they are labeled as “F”. The labeling of each vertex in the adjacency graph consists of three main steps:

**(1) At first, the attribute of each vertex is initialized as “F”, and the corresponding vertex is colored in green, as can be seen from the Figure 3b–e.**

**(2) Grouping the segmented planar patches into different decomposition parts.** In this process, pairs of planar patches that have an edge labeled as “2” are first extracted from the graph generated from above process (Figure 3c). These pairs of planar patches are called anti-symmetry planar patches [12], and they are used to form the initial decomposition parts. This procedure is repeated until all anti-symmetry planar patches are already grouped into the corresponding decomposition parts. As can be seen from Figure 3d, the anti-symmetry planar patches contained in red circles form the different initial decomposition parts. However, there still remain some planar patches that are not contained in any of the initial decomposition parts, such as planar patch one and planar patch 10 shown in Figure 3d. For these planar patches, if they are adjacent to both anti-symmetry planar patches in the initial decomposition parts, they are grouped into the corresponding decomposition parts. As can be seen from Figure 3e, planar patch one is grouped into the decomposition part containing anti-symmetry planar patch two and three, and planar patch 10 is grouped into the decomposition part containing anti-symmetry planar patch eight and nine. Note that the number of planar patches contained in each decomposition part may be different, which is a key cue for the following model recognition in each decomposition part.

**(3) Labeling the vertices that are the anti-symmetry planar patches of the attached part of the main building as “T”.** After aforementioned process, all of the segmented planar patches have been grouped into the corresponding decomposition part. Then, for each pair of anti-symmetry planar patches, if there are planar patches that are adjacent to both of them but not contained in the corresponding decomposition part, the attributes of these anti-symmetry planar patches (the corresponding vertices) are modified as “T”. As can be seen from Figure 3f, for anti-symmetry planar patch two and three, existing planar patch four that is adjacent to both of them but not contained in the decomposition part containing anti-symmetry planar patch two and three. Therefore, the decomposition part containing anti-symmetry planar patch two and three is an attached part of the main building and the attributes of vertex two and three are modified as “T”. The aim of classifying the vertices into “F” and “T” is to identify the attached part of the main building in the sub-graph, which will be described in the following section.

The final graph generated from above process can be seen in Figure 3f. In Figure 3f, the red vertices indicate that the attributes of these vertices are labeled as “T”, and the green vertices indicate that the

attribute of these vertices are labeled as “F”. Such graph is called an attributed graph, which can be used to find the plausible decomposition of compound buildings.

### 2.3.2. Sub-graph Extraction from the Attributed Graph

The process of sub-graph extraction starts by searching pairs of planar patches that have an edge labeled as “2” (anti-symmetry planar patches) in the attributed graph, which are contained in different decomposition parts. Then, the planar patches that are adjacent to any of these anti-symmetry planar patches in each decomposition part are all extracted to form the initial sub-graphs. In this case, the initial sub-graphs may contain some vertices belonging to the attached part of the main building, which affects the generation of the final sub-graph of each decomposition part. Figure 4a shows five initial sub-graphs extracted from the attributed graph shown in Figure 3f. As can be seen from it, for the anti-symmetry planar patches four and five in the decomposition part II, the planar patches that are adjacent to any of them are planar patches two, three, six, seven, eight, and nine. Among these planar patches, planar patch two and three belong to the attached part of the main building, and they are redundant for the decomposition part II in the following model recognition and initial model’s generation. Therefore, these vertices (labeled as “T” in the attributed graph) will be discarded from the decomposition part II to construct the final sub-graph, which can be seen from Figure 4b. Figure 4c shows the final sub-graph of each decomposition part.

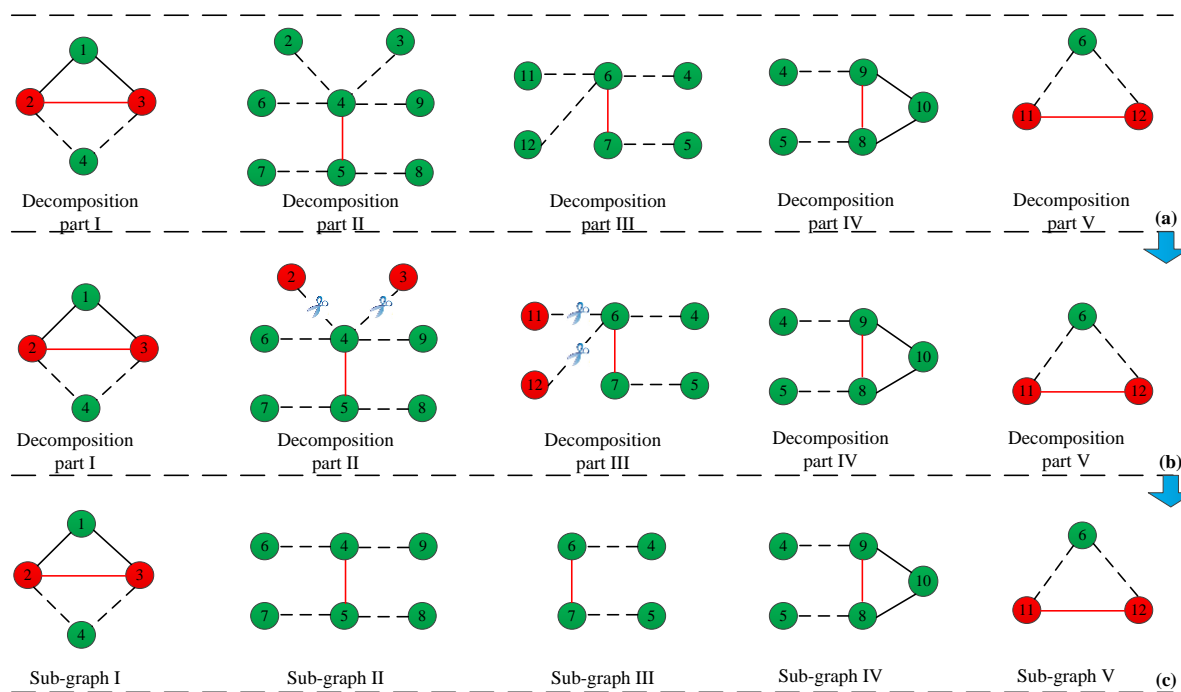


**Figure 4.** Sub-graph extraction from the attributed graph. (a) The initial sub-graphs of different decomposition part; (b) discarding the vertices labeled as “T” from the initial sub-graphs; and (c) final sub-graphs of different decomposition parts. Note that the edge colored in red indicates a ridge line contained in the compound building, the red vertices indicate that the attributes of these vertices are labeled as “T”, and the dotted line in the sub-graphs indicates that the two vertices are adjacent planar patches but one of them is not contained in the corresponding decomposition part.

Note that if the vertices labeled as “T” are the anti-symmetry planar patches in the corresponding decomposition part, they will not be discarded from the initial sub-graph. As can be seen from Figure 4a, planar patch two and three are the anti-symmetry planar patches of the decomposition part I, but not the anti-symmetry planar patches of the decomposition part II (planar patch four and five are the anti-symmetry planar patches of the decomposition part II). Therefore, though the vertex two and three are labeled as “T”, they are reserved in the sub-graph I but discarded from the sub-graph II.

### 2.3.3. Primitive’s Definition and Recognition

After the decomposition of the attributed graph, sub-graphs of different decomposition parts can be derived and used to recognize the primitive’s type. To do that, it is necessary to set up a library of basic building primitives firstly. In this paper, three types of basic primitives are defined for the reconstruction of compound building models with symmetric roofs, and these basic primitives are categorized into three classes with respect to the number of planar patches contained in each decomposition part, which can be seen in Figure 5.

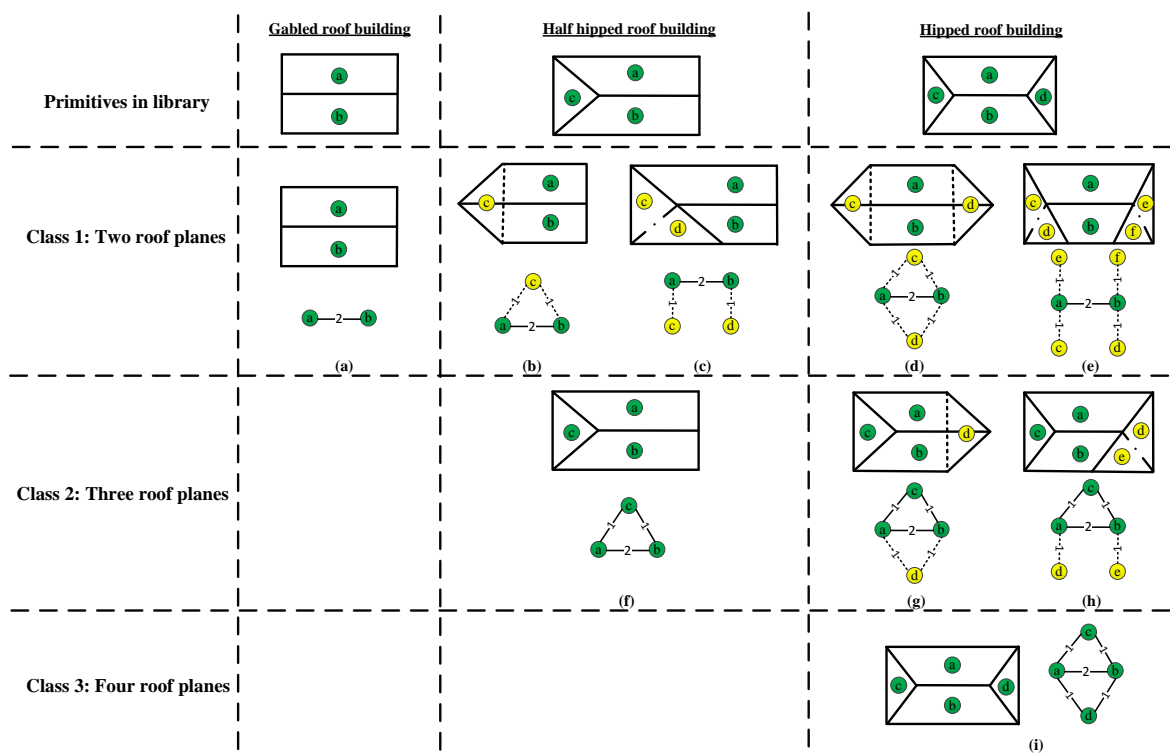


**Figure 5.** Three classes of primitives defined according to the number of planar patches contained in the decomposition part and the corresponding sub-graphs. (a) Gabled roof primitive; (b) half hipped roof primitive with convex shape; (c) half hipped roof primitive with concave shape; (d) hipped roof primitive with convex shape; (e) hipped roof primitive with concave shape; (f) half hipped roof primitive; (g) hipped roof primitive with convex shape; (h) hipped roof primitive with concave shape; and (i) hipped roof primitive. Note that the yellow vertices (connected with the dotted lines in the sub-graphs) indicate that they are adjacent to the anti-symmetry planar patches but not contained in the corresponding decomposition part.

From Figure 5, it can be seen that the primitives in the predefined library are classified into nine types according to the number of planar patches contained in the corresponding decomposition part, and these primitives have different forms of sub-graphs. In this paper, the number of planar patches contained in each decomposition part and the corresponding sub-graph are jointly used to recognize the primitive's type, which can be seen in Figure 6.

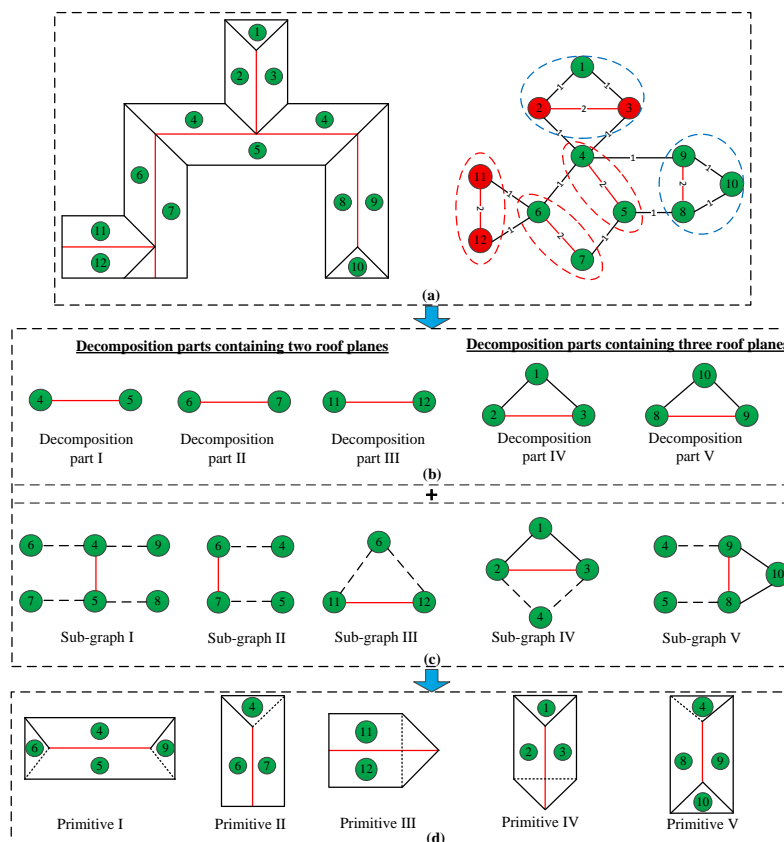


**Figure 6.** The recognition of each primitive in the corresponding decomposition part. (a) A compound building and its attributed graph; (b) the segmented planar patches contained in each decomposition part; (c) the sub-graph of each decomposition part; and (d) the recognized primitive in each decomposition part.

After the construction of the attributed graph, the segmented planar patches have been grouped into the corresponding decomposition part. Figure 6b shows five decomposition parts derived from the attributed graph shown in Figure 6a. It can be seen that the number of planar patches contained in each decomposition part is different, which can narrow down the primitive's recognition to the corresponding class shown in Figure 5. Subsequently, once the sub-graph of each decomposition part has been extracted from the attributed graph (Figure 6c), the corresponding model type can be recognized by sub-graph matching (Figure 6d). As can be seen in Figure 6b, there are two planar patches contained in the decomposition part I–III, so the recognition of these primitives are first narrowed down to Class 1 shown in Figure 5. Then, these primitives are recognized by the sub-graph matching: For sub-graph I, there are four planar patches adjacent to the anti-symmetry planar patches, it is a hipped roof that corresponds to the primitive shown in Figure 5e; for sub-graph II, there are two planar patches adjacent to the anti-symmetry planar patches respectively, it is a half-hipped roof that

corresponds to the primitive shown in Figure 5c; for sub-graph III, there is only one planar patch adjacent to both anti-symmetry planar patches, it is a variant of half hipped roof building that corresponds to the primitive shown in Figure 5b. The aforementioned recognition method can also be applied to the decomposition part containing three roof planes. For example, there are two planar patches adjacent to both anti-symmetry planar patches in sub-graph IV, it is a variant of hipped roof that corresponds to the primitive shown in Figure 5g.

Note that the proposed method allows the overlapping of neighboring primitives in the recognition process, which is achieved by analyzing the corresponding sub-graph of each decomposition part. As can be seen from Figure 7, part of compound building shown in Figure 6a is decomposed into three overlapping primitives by using the proposed semantic decomposition algorithm. Such decomposition has two main advantages in the following reconstruction process. First, it reduces the number of primitives defined in the library. If the compound buildings are decomposed into some non-overlapping decomposition parts, the intersection of neighboring primitives will produce another primitive with various forms, which are difficult to be defined and reconstructed. Another advantage of such decomposition is that it keeps the primitive’s integrity and regularity during the semantic decomposition. As a result, each decomposed primitive can be represented by a few parameters, which allows the quite robust parameter estimation in the following reconstruction.

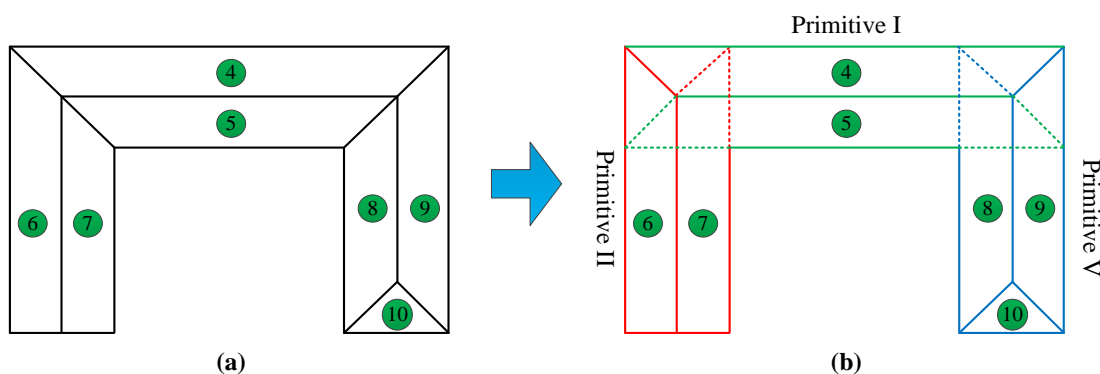


**Figure 7.** Semantic decomposition allowing the overlapping of neighboring primitives. (a) A compound building; and (b) decomposition result of the proposed method.

### 2.3.4. Generation of Initial 3D Building Primitives

Once the primitives have been recognized, the approximate reconstruction of each initial 3D primitives can be performed based on the primitive’s type and the corresponding planar patches. The generation of the initial 3D primitives is essential because it provides the initial value for the primitive’s parameter optimization in the following reconstruction process and a relatively smaller search space to find the corresponding features in the aerial imagery. In this paper, a novel initial 3D building model generation algorithm is proposed based on Minimum Bounding Rectangle (MBR) and the attributed graph, which is described as follows:

**(1) Derivation of the 2D MBR of each decomposition part.** Once the decomposition of compound buildings has been completed, the approximate 2D outline of each decomposed primitive can be derived by using a MBR algorithm [46]. More specifically, the planar patches contained in each

decomposition part are projected onto the XY plane to derive the convex hull, and then the 2D MBR is determined by the rectangle with minimum area that contains all the 2D convex hull points. The MBRs of two decomposed primitives can be seen in Figure 8, which are colored in yellow. The utility of the 2D MBR is that it can provide the approximate 2D eave corners (corners (1–4) in Figure 8) of each decomposed primitive, which is crucial for the generation of initial 3D primitives. In addition, the 2D MBR can be used to determine the initial parameters and the main orientation of each decomposed primitive, which is necessary for the subsequent reconstruction steps.

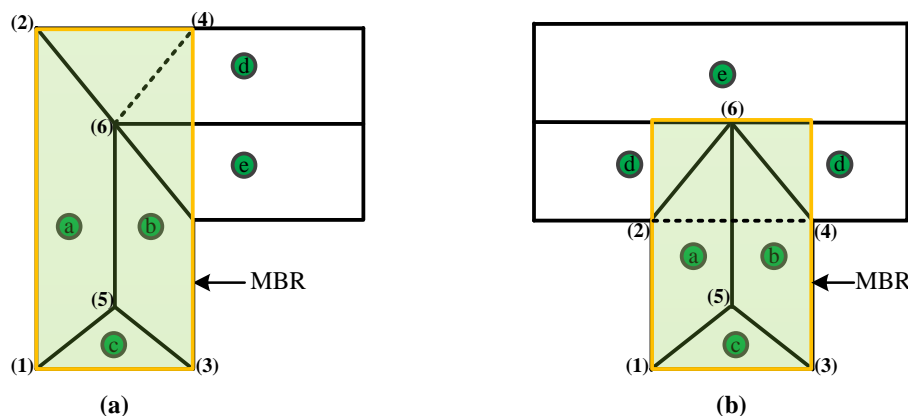


**Figure 8.** The generation of initial 3D primitives using MBRs and the corresponding planar patches. (a) The generation of initial 3D primitives with concave shapes; and (b) the generation of initial 3D primitives with convex shapes.

**(2) Generation of the initial 3D primitives.** To derive the initial 3D primitives, the approximate 3D corners of each primitive should be calculated. In this study, 3D corners of primitives are classified as eave corners (corners (1–4) in Figure 8) and ridge corners (corners (5–6) in Figure 8) because they are calculated by using different methods. For ridge corners, they are calculated by the intersection of concurrent planar patches. For example, 3D coordinates of the corner (5) in Figure 8 can be calculated by the intersection of planar patch a, b, and c. However, the 3D eave corners cannot be calculated by the intersection of 3D planes because the wall planes are absent. In this case, the 2D MBRs can substitute the walls to provide the approximate 2D eave corners ( $x_i, y_i$ ) of each decomposed primitive, and then the 3D eave corners can be calculated by using the 2D eave corners and the corresponding 3D plane equation. As can be seen from Figure 8a, 3D coordinates of the eave corners (1–2) can be calculated by using the 2D eave corners ( $(x_1, y_1), (x_2, y_2)$ ) and the 3D plane equation of planar patch a.

However, the 3D eave corners of basic primitives with convex shapes may not be located at the corners of the MBR, which can be seen in Figure 8b. In this case, corner (2) and corner (4) cannot be calculated using the MBR and the corresponding 3D planes. To address this problem, a 3D plane (*bottom plane*) is first estimated using the 3D coordinates calculated from the MBR and anti-symmetry planar patches, and then the 3D eave corner can be derived using this *bottom plane* and two adjacent planes. For example, 3D eave corner (2) in Figure 8b can be derived by the intersection of planar patch a, d and the estimated *bottom plane*. Note that the primitive’s type determines the calculation method of the 3D eave corners. For example, the 3D eave corners of primitive (b), (d), and (g) in Figure 5 are

calculated by using the method illustrated in Figure 8b, and the 3D eave corners of other primitives are calculated by using the method illustrated in Figure 8a.

#### 2.4. Image Feature Extraction and Building Modeling

The main idea of the proposed method is to decompose compound buildings into basic building primitives, and then each building primitive is reconstructed using the constraints from LiDAR data and aerial imagery. In this process, the relevant features should first be extracted from the LiDAR data and aerial imagery to form the cost function, and then a non-linear least squares optimization is performed to reconstruct the building model. In this study, the features from LiDAR data are the segmented planar patches which have been extracted by RANSAC, and the features from the perspective aerial imagery are the 2D image corners of each building primitive which can be derived depending on the initial 3D building primitives generated from above process.

##### 2.4.1. Feature Extraction from Perspective Aerial Imagery

Using the known orientation parameters of the aerial imagery, the initial building primitives derived from LiDAR data can be projected onto the corresponding aerial imagery, which can be seen in Figure 9a. It can be seen that, the back projected wireframe provides a relatively smaller searching space to find the corresponding features in the aerial imagery. Thus, a buffer is constructed from the initial building's boundary to derive a sub-image, and then the corner extraction procedure is conducted on this sub-image as follows:

(1) The discrete edge pixels are first detected by applying a canny edge detector [47] on the sub-image where the initial building primitive appears, followed by linking edge pixels to derive line segments. Then, line segments whose lengths are smaller than a given threshold are removed. The resulting edge map is shown in Figure 9b. It can be observed that there are still too many edge pixels in the building region and it is hard to find the correct building edges.

(2) To filter the irrelevant edge pixels, buffer regions are generated based on each back projected edge of the initial model (pairs of red dot lines in Figure 9c), and only the edge pixels that are inside the defined buffer are considered as candidate edge pixels. The buffer size is set according to the point spacing of the LiDAR point cloud. Figure 9c shows the edge pixels located in each buffer region of an initial hipped roof model; different colors represent different groups of edge pixels in the buffer zone.

(3) As seen in Figure 9c, there are many edge pixels that do not belong to the actual building boundaries still reserved in each buffer, so the RANSAC algorithm [48] is applied to each group of edge pixels to filter irrelevant edge pixels again, and then the inliers can be used to estimate the equations of 2D straight lines. The result can be seen in Figure 9d; pixels with different colors indicate different groups of inliers.

(4) During back projection, the geometry and topology of the initial building primitives are transformed into two dimensional features, and the topological relationships between them are preserved. That is, once the primitive's type is determined, the relationships among the corners and the corresponding model edges are available from a 3D initial model reconstructed from LiDAR data. Consequently, after the straight lines have been derived from the aforementioned steps, the 2D corners

of each building primitive can be extracted by the intersection of neighboring straight lines, which can be seen in Figure 9e.

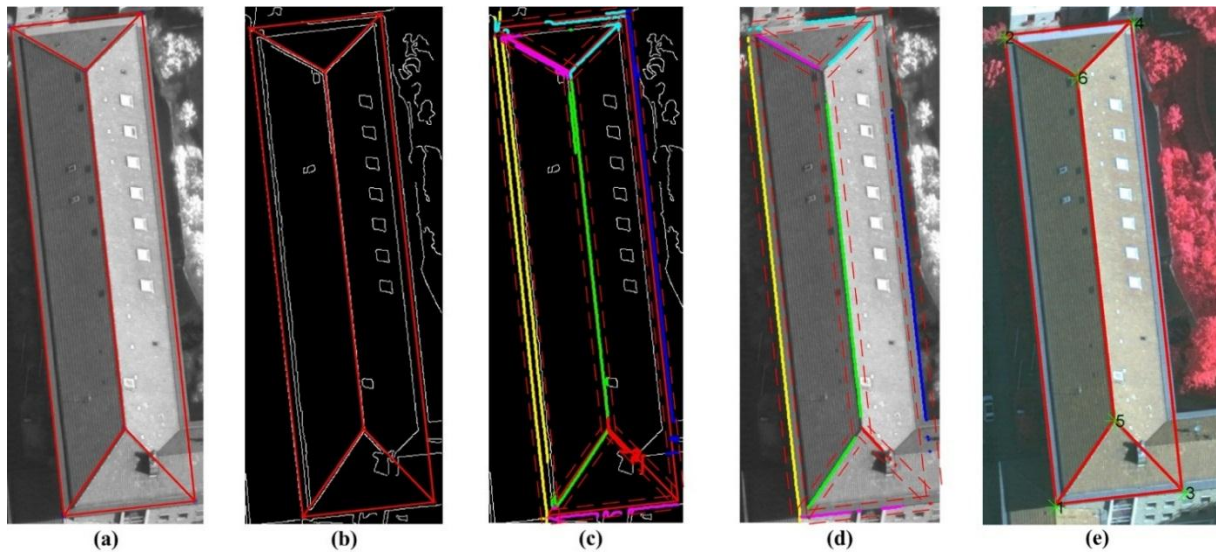


**Figure 9.** The process of corner extraction from aerial imagery. (a) Initial model back projected onto the corresponding aerial imagery; (b) initial model superimposed onto the edge map; (c) edge pixels in the buffer zone; (d) inliers of RANSAC superimposed onto the gray image; and (e) the extracted 2D corners.

#### 2.4.2. Building Modeling Using Constraints from LiDAR Data and Perspective Aerial Imagery

After the aforementioned process, both the planar patches and the accurate 2D image corner of each building primitive can be acquired, together with the primitive’s type and initial parameters, the accurate 3D building primitives can be derived by using a primitive-based reconstruction algorithm proposed by Zhang *et al* [41]. In this method, two constraints from LiDAR data and aerial imagery are used for the reconstruction of each building primitive. First, the back-projections of the 3D primitive’s vertices onto the aerial image should perfectly superpose onto the extracted corners; this constraint can be expressed by the collinearity equation. Second, the primitive’s vertices should be exactly on the 3D planes extracted from LiDAR point clouds; this constraint can be expressed by the point-to-plane distance. According to these constraints, the observation functions can be established as Equation (1).

$$\begin{aligned}
 x_i &= x_p - f \frac{a_1(X_i - X_S) + b_1(Y_i - Y_S) + c_1(Z_i - Z_S)}{a_3(X_i - X_S) + b_3(Y_i - Y_S) + c_3(Z_i - Z_S)} \\
 y_i &= y_p - f \frac{a_2(X_i - X_S) + b_2(Y_i - Y_S) + c_2(Z_i - Z_S)}{a_3(X_i - X_S) + b_3(Y_i - Y_S) + c_3(Z_i - Z_S)} \\
 d_i &= |AX_i + BY_i + CZ_i + D| / \sqrt{A^2 + B^2 + C^2}
 \end{aligned}
 \tag{1}$$

where,  $x_i, y_i$ : Projected image coordinates of the 3D primitive’s vertex  $i$ ;  $x_p, y_p, f$ : Image coordinates of the principle point and the principle distance;  $X_i, Y_i, Z_i$ : 3D coordinates of the primitive’s vertex  $i$  in the object coordinate system;  $X_S, Y_S, Z_S$ : 3D coordinates of the perspective center in the object coordinate

system;  $\begin{bmatrix} a_1 & b_1 & c_1 \\ a_2 & b_2 & c_2 \\ a_3 & b_3 & c_3 \end{bmatrix}$ : the elements of the rotation matrix that depend on the rotation angles;  $d_i$ : the distance of a 3D primitive's vertex  $i$  to the corresponding 3D roof plane;  $A, B, C, D$ : plane parameters that can be estimated from the 3D points located on the same 3D roof plane.

Note that the 3D coordinates of each primitive's vertex  $(X_i, Y_i, Z_i)$  in Equation (1) can be calculated by the shape parameters and pose parameters, which are the unknown parameters that need to be optimized. In this paper, the shape parameters are used to describe the shape and size of the primitive, and the pose parameters define three translation parameters  $(X_m, Y_m, Z_m)$  and three rotation parameters  $(\omega_m, \varphi_m, \kappa_m)$  of the primitive relative to the object coordinate system. For example, the unknown parameters of a gabled roof primitive are pose parameters  $(X_m, Y_m, Z_m, \omega_m, \varphi_m, \kappa_m)$  and shape parameters  $(l, w, h)$ .  $l$  and  $w$  refer to the length and width of the gabled roof,  $h$  refers to the height of the roof ridge relative to  $Z_m$ . Using shape parameters, we can derive the vertex's coordinate  $(U_i, V_i, W_i)$  of the gabled roof primitive in the model coordinate system, which can be seen in Figure 10.

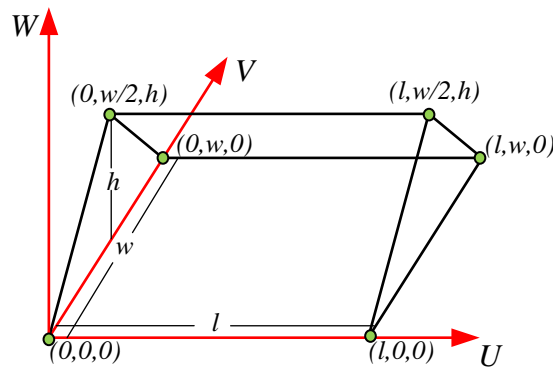


**Figure 10.** The model coordinates of the gabled primitive's vertices calculated by shape parameters.

When transforming the primitive from the model coordinate system  $(UVW)$  to the object coordinate system  $(XYZ)$ , three translation parameters  $(X_m, Y_m, Z_m)$  and three rotation parameters  $(\omega_m, \varphi_m, \kappa_m)$  are used, which can be expressed as Equation (2).

$$\begin{bmatrix} X_i \\ Y_i \\ Z_i \end{bmatrix}_{object} = \begin{bmatrix} X_m \\ Y_m \\ Z_m \end{bmatrix}_{object} + R_{model}^{object}(\omega_m, \varphi_m, \kappa_m) \begin{bmatrix} U_i \\ V_i \\ W_i \end{bmatrix}_{model} \tag{2}$$

Based on the aforementioned transformation, the constraints of a gabled roof expressed in Equation (1) can be formulated as:

$$\begin{cases} x_i = f_x(X_m, Y_m, Z_m, \omega_m, \varphi_m, \kappa_m, l, w, h) \\ y_i = f_y(X_m, Y_m, Z_m, \omega_m, \varphi_m, \kappa_m, l, w, h) \\ d_i = f_d(X_m, Y_m, Z_m, \omega_m, \varphi_m, \kappa_m, l, w, h) \end{cases} \tag{3}$$

Using these constraint equations, the cost function to be minimized can be formulated as Equation (4):

$$\sum (x_i - x_i')^2 + \sum (y_i - y_i')^2 + \sum (d_i)^2 \rightarrow min \tag{4}$$

In Equation (4),  $(x_i, y_i)$  is the back projected image coordinates of the primitive's vertex  $i$ , which can be calculated by the collinearity equation;  $(x'_i, y'_i)$  is the image coordinate of the primitive's vertex  $i$ , which can be derived by corner extraction from aerial imagery;  $d_i$  is the distance of a primitive's vertex  $i$  to the corresponding roof surface. Starting from the initial values of the shape and pose parameters, the optimal parameters can be determined by using a non-linear least squares optimization. In this paper, the LM (Levenberg-Marquardt) non-linear least squares optimization algorithm [49] is used to optimize the cost function. Finally, 3D buildings can be represented using the optimized shape and pose parameters. By this means, the constraints from LiDAR data and aerial imagery can be tightly integrated into a parameter optimization procedure to derive the accurate 3D building primitives.

### 3. Experimental Results

#### 3.1. Description of the Datasets

Two datasets containing the LiDAR point cloud and aerial imagery were used in our experiments to validate the proposed method. The "Vaihingen" dataset was provided by the ISPRS test project on urban classification and 3D building reconstruction [50], which was acquired by the Leica ALS50 system with an average point density of 4 points/m<sup>2</sup> at a mean flying height of 500 m above ground level. Multispectral aerial images were also captured from the Intergraph Z/I imaging's DMC (Digital Mapping Camera) with a GSD (Ground Sampling Distance) of 8 cm.

The Strasbourg dataset was obtained in 2004 using the Optech ALTM 1225 with an average height of 1440 m, and the point density is approximately 1.3 points/m<sup>2</sup>. Aerial images that were acquired using a Vexcel UltraCamX with a GSD of 15 cm were also contained in the Strasbourg dataset. For the aforementioned two datasets, the interior and exterior parameters were also distributed with the corresponding aerial images.

#### 3.2. Experimental Results

In the previously mentioned datasets, a total of eight representative buildings are selected to validate the proposed method. Among these buildings, there are seven compound buildings, which are characterized by a combination of basic building primitives. Figure 11 shows the decomposition and reconstruction results of these compound buildings. In addition, there is also a complex flat roof building in the test data, which can be seen in Figure 12.

As seen in Figure 11, the compound buildings in Part (i) can be automatically decomposed into some semantic primitives defined in the library, e.g., the complex building in Figure 11a can be automatically decomposed into three hipped building primitives. Figure 11 (Part ii) shows the decomposition results of different compound buildings; wireframes in different colors indicate different building primitives derived from the proposed decomposition method, and points in different colors represent different segmented planar patches. Once the compound buildings have been decomposed into basic primitives and the corresponding features have been extracted from LiDAR data and aerial imagery, the reconstruction of the building models can be achieved by using a non-linear least squares optimization.

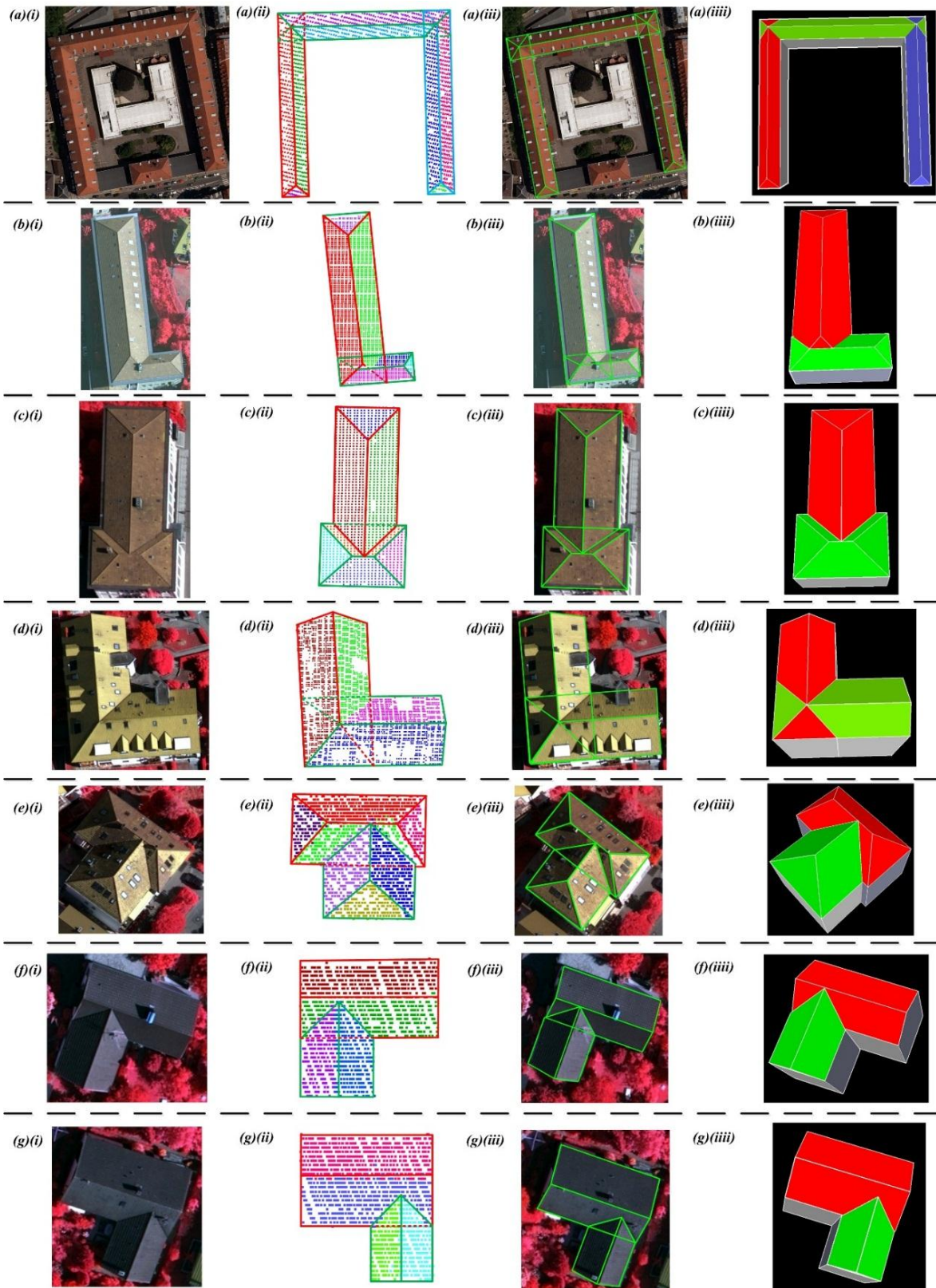


**Figure 11.** Experimental results of the proposed method. Parts (a–g): the selected seven compound buildings for the experiments; and parts (i–iiii): aerial imagery, decomposition results, and the initial roof models (wireframes in different colors indicate different decomposed primitives), back projections of the reconstructed models (green wireframes), and 3D visualization of the reconstructed models.

For a qualitative evaluation of the proposed method, the reconstructed 3D building models are back projected to the corresponding aerial imagery, which are shown in Figure 11 (Part iii). As can be seen from it, the 2D green wireframes superimposed on the aerial images are the projections of the 3D reconstructed building models; they are located at their correct locations and coincide well with the corresponding building edges on the aerial imagery, which means that the proposed method can generate accurate building models. When the roof models have been reconstructed, the complete 3D building models can be derived by extruding the roof outline to the ground when a DEM is available, or to a ground plane with a given height. Figure 11 (Part iiiii) shows the 3D visualization of the reconstructed building models, models with different colors indicate different reconstructed primitives.

Note that there are also some complex building roofs that do not contain ridge lines in a real urban environment; an example can be seen in Figure 12a, which is a complex flat roof building with a polygonal shape. In this case, the proposed decomposition algorithm cannot work to reconstruct these complex buildings. For this type of building, a polygonal model is designed, and then the constraints from the 2D image corners and 3D planar patches from LiDAR data are used to reconstruct this polygonal building model [41]. This procedure is illustrated in Figure 12.

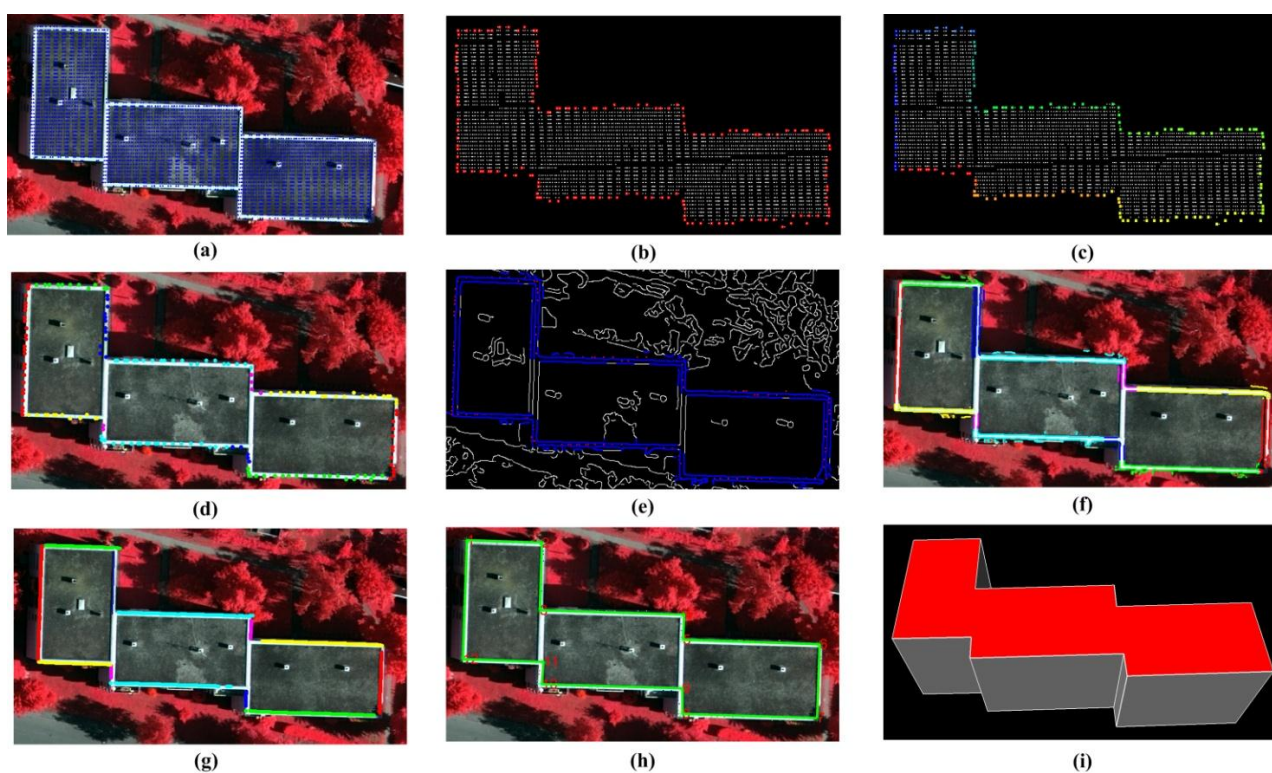


**Figure 12.** Reconstruction of a complex flat building with polygonal shape. (a) The segmented planar patch of a complex flat roof (blue points); (b) the extraction of 3D boundary points (red points); (c) the grouping result of the 3D boundary points; (d) the grouping boundary points that are back projected onto the aerial imagery; (e) edge detection on the sub-image; (f) edge pixels in the neighborhood of the back-projected boundary points; (g) inliers of the RANSAC; (h) results of 2D corner extraction; and (i) the reconstructed 3D flat building model.

After rooftop segmentation, the LiDAR points located on the same plane at different elevation levels can be extracted, and the 2D image corners of each building can be detected with the help of these planar patches using the following steps. First, the 3D boundary points of each planar patch are obtained by using the modified convex hull method [51], and then these 3D boundary points are grouped into different groups by using sleeve algorithm [14]. Red points shown in Figure 12b are the extracted 3D boundary points and Figure 12c shows different group of boundary points. Second, the grouped 3D boundary points were projected back to the aerial imagery and the canny detector was applied to the aerial imagery to derive the 2D edge pixels. A buffer (15 pixels, indicating approximately two times the point spacing) surrounding these projected boundary points was defined to find the corresponding 2D edge pixels on the image. These are demonstrated in Figure 12d and Figure 12e. Finally, the RANSAC algorithm was applied to each group of 2D edge pixels (Figure 12f) to filter the irrelevant edge pixels and derive straight lines (Figure 12g), and then 2D corners can be extracted by the intersection of the neighboring straight lines, which can be seen in Figure 12h. Once the 2D corners have been extracted from the aerial imagery, the type of the corresponding polygonal building model is known, and then accurate building models can be derived by using constraints from aerial imagery and the corresponding LiDAR planar patch. Figure 12i shows the final 3D building model reconstructed from the aforementioned procedure.

## 4. Discussions

### 4.1. Comparison Analysis of the Proposed Semantic Decomposition Method

In this section, four related building reconstruction methods based on roof topology graphs are compared with the proposed method according to the decomposition results, and the different decomposition results of the same compound building are used to illustrate the novelty of the proposed method, which can be seen from Figure 13. Figure 13 (left) shows the rooftop segmentation results, the number of the segmented planar patches and the corresponding roof topology graph, and Figure 13 (right) shows the different decomposition results (planar patches contained in each decomposition part) and the reconstructed 3D building models.

Seo [12] extracted wing models from LiDAR data by analyzing the surface patch adjacency graphs, and then aggregated these wing models for the reconstruction of complex buildings. As can be seen from Figure 13a, the wing models used in this method were only the combination of planar patches, but not semantic building primitives that were familiar to people. Thus, they cannot be represented as parametric forms to adopt a model-driven method for the reconstruction. To extract parametric models from the LiDAR points, Verma *et al.* [22] defined simple roof shapes as  $G_I$ ,  $G_L$ , and  $G_U$  models, which can be recognized by the corresponding sub-graphs. These simple roof shapes were searched from the roof topology graphs and then reconstructed by fitting them to the point clouds. For the compound building model in Figure 13, the decomposition result is a  $G_U$  shape model in Verma *et al.* [22], which is still a combination of basic building primitives (Figure 13b). This decomposition will reduce the flexibility of the building reconstruction because it needs to define a more complicated building primitive and then extract it using an exhaustive search.

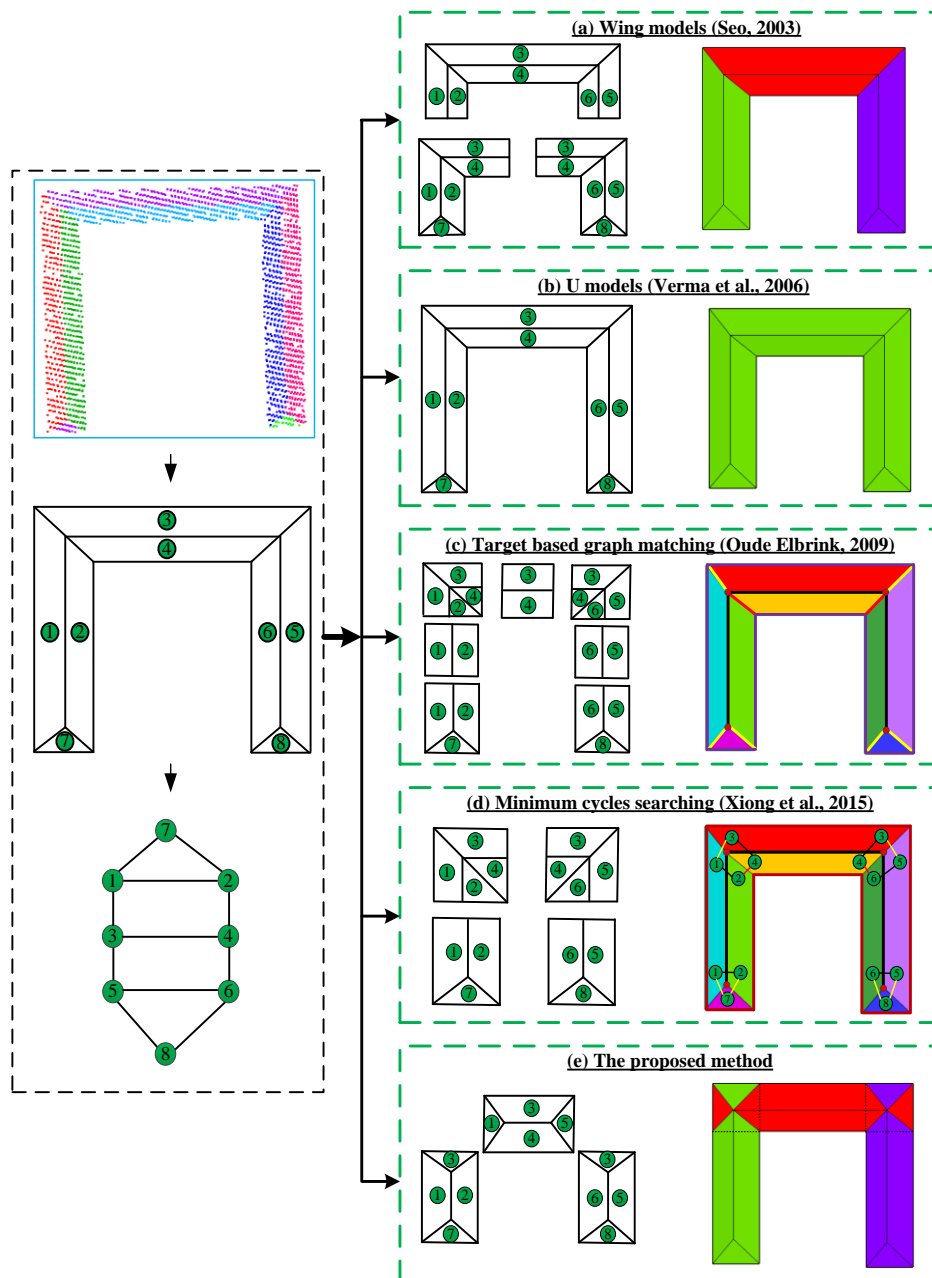


**Figure 13.** Decomposition results of different building reconstruction methods using roof topology graph. **Left:** the rooftop segmentation results, the number of the segmented planar patches and the corresponding roof topology graph. **Right:** the decomposition results and the reconstructed 3D building models. **(a)** The decomposition result of the reconstruction method proposed by Seo [12]; **(b)** the decomposition result of the reconstruction method proposed by Verma *et al.* [22]; **(c)** the decomposition result of the reconstruction method proposed by Oude Elberink and Vosselman [37]; **(d)** the decomposition result of the reconstruction method proposed by Xiong *et al.* [52]; and **(e)** the decomposition result of the proposed method.

In the paper of Oude Elberink and Vosselman [37], airborne laser scanner data and an existing 2D map were used to reconstruct building models based on a target-based graph matching algorithm. The decomposition result of this method was the assignment of a target graph to the corresponding planar

patch and intersection lines, which will result in redundancy because the segmented planar patches and the corresponding intersection lines might have matched with multiple targets. As can be seen from Figure 13c, the decomposition results of this method were three gabled roofs, two half-hipped roofs and two L-shaped roofs. In addition, these primitives are not semantic primitives with fixed parametric description, but the group of intersection lines and the corresponding planar segments. Based on the same roof topology graph, Xiong *et al.* use flexible building primitives (loose nodes, loose edge, and minimum cycles) for 3D building reconstruction [52]. By searching minimum cycles from the roof topology graph, the inner corners can be detected and calculated by intersecting the concurrent planes (Figure 13d), and then the outer corners were computed by assuming horizontal or vertical planes using boundary points. Finally, the complete building model can be derived by linking all inner corners and outer corners. Using corners as basic primitives is flexible for building reconstruction, but it is usually difficult to determine the topological relationship of different corners and the linking lines. In addition, building models generated from these methods are geometric models, but the semantic information about the building's type is always missed in the reconstruction process.

Differing from the aforementioned method, the results of the proposed automatic decomposition algorithm are semantic building primitives, which can be easily interpreted by the architects. As can be seen from Figure 13e, the decomposition results of the proposed method are three hipped roofs, which have semantic information about the building's type. Such decomposition is much simpler and can be easily accepted by human being. In addition, each semantic building primitive used in this paper can be represented by a parametric form, which reduces the model parameters and facilitates the integration of aerial imagery in the following reconstruction process. Furthermore, the results of the proposed decomposition method are basic building primitives allowing overlapping in the reconstruction procedure. Such decomposition and reconstruction are more flexible because only a small set of simple building primitives need to be contained in the predefined library.

#### 4.2. Analysis of the Sub-Graph Searching and Initial Primitive's Generation

Among most decomposition methods using sub-graph matching, the process of searching sub-graph in the roof topology graph is complex. That is to say, for each predefined primitive, the corresponding sub-graph is searched in a certain order, such as in a decreasing order of complexity of primitives [22]. In this case, it is usually an exhausting search. By contrast, the searching of basic primitives in this paper is more efficient than the aforementioned methods. It is explained by the fact that the anti-symmetry planar patches can be easily extracted from the attributed graph, and then the relevant planar patches that are adjacent to these anti-symmetry planar patches are efficiently retrieved to constitute a sub-graph, which can avoid the exhausting sub-graph searching in the roof topology graph.

After identifying of sub-graphs in the roof topology graph, the ridge corners can be calculated by the intersection of concurrent planar patches. To achieve the complete models, building outlines should be determined in most reconstruction methods. In this process, the building outlines are derived either by extraction and regularization of boundaries or by auxiliary horizontal and vertical planes, and then the initial building model is generated based on the derived ridge corners and building outlines. This process is usually complicated because it needs to reconstruct the complex topology relationship between line segments that are linked by the corners. In this paper, this complexity is reduced by

decomposing the compound building into simple building primitives with inherent topology relationships among corners, line segments, and planes. As a result, the outline of each decomposed primitive can be easily derived by using MBR algorithm, and then these initial 3D primitives can be easily generated based on the primitive’s type, the corresponding planar patches and the 2D MBR.

### 4.3. Accuracy Assessments of the Reconstructed Building Models

The geometric accuracy of the reconstructed building models is evaluated in two ways. First, we compare the coordinates of the reconstructed roof corners with the ones acquired by space intersection using stereo images and calculate the RMSE (Root-Mean-Square Error) of each primitive, which can be seen in Figure 14a. In Figure 14 a, the maximum RMSE in the horizontal direction is smaller than 0.25 m, and the maximum RMSE in the vertical direction is smaller than 0.20 m. For the total of sixteen building primitives, the average RMSE values are 0.11 m and 0.12 m in the horizontal and vertical directions, respectively, which indicate that the proposed building reconstruction method has high geometric accuracy in both the horizontal and vertical directions. Second, the distances from the LiDAR point clouds to the reconstructed roof are calculated to validate the reconstructed errors, which can be seen in Figure 14b. In Figure 14b, the standard deviation and the mean of the distances from the LiDAR points to the corresponding 3D building model are smaller than 0.07 m in most cases, which proves the high vertical accuracy of the reconstructed building model. Note that the vertical accuracy evaluated by the LiDAR point clouds is higher than that evaluated by the space intersection. This inconsistency may be originated from the manual work during the measurement of 2D image corners from stereo images.

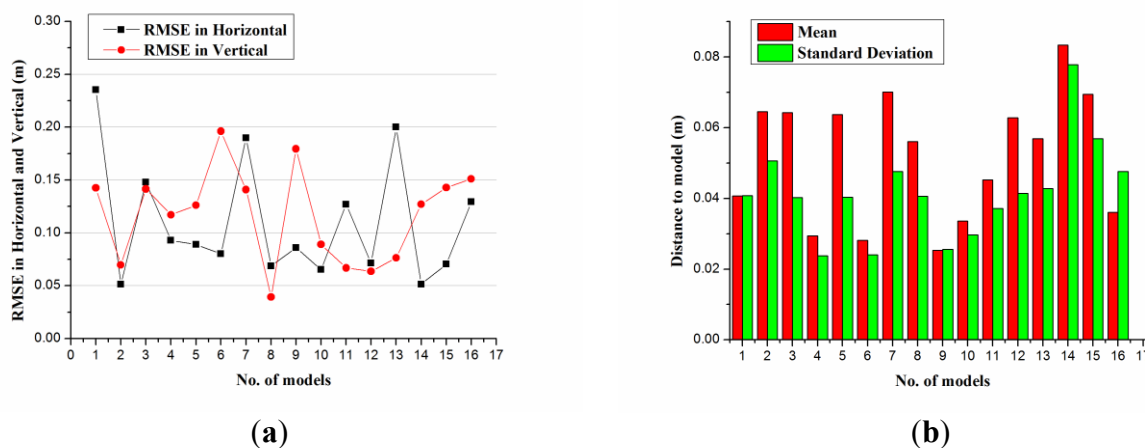


**Figure 14.** Accuracy assessment of the proposed method. (a) RMSE of the reconstructed building model in the horizontal and vertical directions; and (b) mean and standard deviation of the distances from the LiDAR point clouds to the reconstructed building models.

In addition to the reconstruction of the aforementioned represented buildings, the proposed method is applied to data sets of the ISPRS benchmark [53], which contain three test areas with different characteristics. The organizer of this ISPRS Test Project maintains the web page that shows the continuous comparison of different methods [54], and the geometric accuracy comparison result of different reconstruction methods is presented in Table 1. In this table, RMSD refers to average root

mean square error in the XY plane and RMSZ refers to average root mean square error in the Z direction. The result of the proposed method is highlighted in green.

**Table 1.** Geometrical accuracy of different reconstruction methods in three test areas.

Researchers and References	Area 1		Area 2		Area 3	
	RMSD (m)	RMSZ (m)	RMSD (m)	RMSZ (m)	RMSD (m)	RMSZ (m)
J.Y. Rau [55]	0.9	0.6	0.5	0.7	0.8	0.6
Oude Elbrink and Vosselman [37]	0.9	0.2	1.2	0.1	0.8	0.1
Xiong <i>et al.</i> [39]	0.8	0.2	0.5	0.2	0.7	0.1
Perera <i>et al.</i> [40]	0.8	0.2	0.3	0.3	0.5	0.1
Dorninger and Pfeifer [9]	0.9	0.3	0.7	0.3	0.8	0.1
Sohn <i>et al.</i> [56]	0.8	0.3	0.5	0.3	0.6	0.2
Awrangjeb <i>et al.</i> [19]	0.9	0.2	0.7	0.3	0.8	0.1
He <i>et al.</i> [57]	0.7	0.2	0.6	0.3	0.7	0.2
The proposed method	0.8	0.3	0.5	0.3	0.6	0.1

As shown in Table 1, the average horizontal error and vertical error of the proposed method in three test areas are 0.8 m and 0.3 m (Area 1), 0.5 m and 0.3 m (Area 2), 0.6 m and 0.1 m (Area 3), respectively. Though the elevation accuracy (RMSZ) is comparable with other reconstruction methods, the plane accuracy (RMSD) of the proposed method outperforms most of other reconstruction methods. It is because the accurate features derived from aerial imagery can be tightly integrated into a parameter's optimization by decomposing the compound buildings into basic building primitives.

#### 4.4. Uncertainties and Limitations of the Proposed Method

The rooftop segmentation results are important inputs for the subsequent building decomposition and modeling. When the RANSAC algorithm is implemented in an iterative way to extract planar patches, some LiDAR points that are not really located on the same plane can be detected. As seen in Figure 15a, the green colored LiDAR points in the red circle are really located on the purple planar patch, but are grouped into the green planar patch because the classic RANSAC algorithm only considers the pure mathematical principle of the plane. In this case, the normal vector consistency validation of the points on the extracted plane is applied. That is, the points on the extracted plane are fit by the least-squares method, and then the discrepancy between the normal vector of each point and the fitting plane is calculated. If the discrepancy is smaller than a predefined threshold, the point is reserved in this planar patch. Otherwise, the point may be located on other rooftop patches and will be put into the original building cluster for the following planar patch extraction. After the normal vector consistency validation, the green LiDAR points in the red circle can be correctly grouped into the corresponding planar patch, which can be seen in Figure 15b. Another problem of the rooftop segmentation is that the extracted points are on the same mathematical planes, but are spatially separated, as seen in the red rectangle in Figure 15c. Such coplanar patches can be separated by a connected component analysis, as seen in Figure 15d.

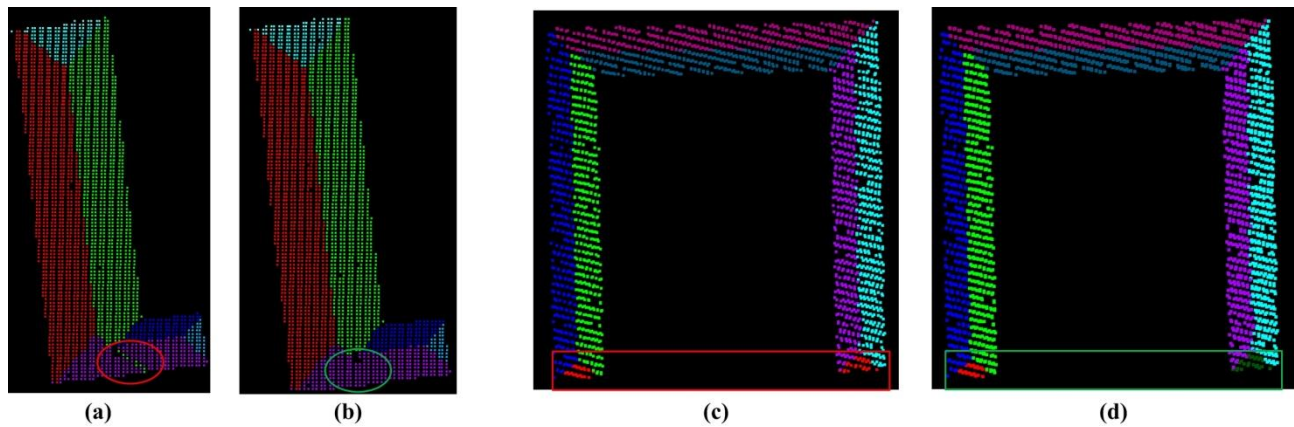


**Figure 15.** Normal vector consistency validation (a–b) and coplanar validation (c–d).

In this paper, a semantic decomposition algorithm is proposed for the automated decomposition of compound buildings, which are suitable for the combination of the gabled roof building, half-hipped roof building, and the hipped roof building. However, the proposed method has limitations when it is used to reconstruct the compound buildings with arbitrary roof orientations, such as the mansard roof buildings. For these buildings, the pairs of anti-symmetry planar patches are absent in the building structure, thus they cannot be decomposed and reconstructed by the proposed method currently. In the future, we will add more complex building primitives for the generalization of the proposed method.

Another limitation of the proposed method is that it has a relatively high computation complexity when it is used to reconstruct a large scene. It is because that the outputs of the proposed method are semantic models but not geometric models, so the semantic decomposition and model recognition have been integrated into the process of the building reconstruction. These processes will increase the computational cost of the proposed method. In addition, the feature extraction from LiDAR data and aerial imagery also have their own computational costs.

## 5. Conclusions

In this paper, an automatic decomposition and modeling method is presented to reconstruct the compound buildings from LiDAR data and aerial imagery. By exploiting the knowledge about local symmetries implicitly contained in the building structure, the proposed method automatically decompose the compound buildings into several semantic building primitives, and then the complementary characters of LiDAR data and aerial imagery are efficiently integrated for the reconstruction of compound building models. The proposed method is tested on two data sets with different point densities, and the quantitative evaluation shown in Figure 14 and Table 1 demonstrate that it can efficiently reconstruct compound building models with higher geometric accuracy.

The proposed approach is a primitive-based technique, in which compound buildings can be decomposed and reconstructed by using a set of simple building primitives. To this aim, a novel decomposition algorithm is proposed to decompose the compound building models into semantic building primitives with fixed parametric forms, which are useful for the architects to interpret the structural components of the compound buildings and then build them using a CSG approach. The benefit of this algorithm is that it can simplify the reconstruction process of the compound building models, especially for the generation of compound buildings that are combinations of gabled or hipped

roofs. In addition, the proposed method allows the basic primitives to overlap in the decomposition process, which can reduce the number of basic primitives in the predefined library and keep the primitive's integrity and regularity during the building reconstruction. As a result, the traditional model driven methods can be further extended to the automated reconstruction of compound buildings by using the proposed semantic decomposition method.

However, it is still a difficult task to automatically reconstruct building models with more complex structures. In this paper, the compound buildings are assumed as a combination of simple primitives with symmetric planar patches, which are not enough for the reconstruction of a variety of complex buildings in reality. In the future, the non-planar roof primitives (e.g., curved structure buildings, cones, and cylinders) will be adopted to extend the proposed method to reconstruct more complex buildings, and the ground-based and mobile-based data will be integrated with the airborne data to create more completed building models.

### Acknowledgments

This work is supported by National Natural Science Foundation of China Grant No. 41171265, 41331171 and 40801131. This work is also supported by the National Basic Research Program of China (973 Program) Grant No. 2013CB733402 and the Open Research Fund of Key Laboratory of Digital Earth Science, Institute of Remote Sensing and Digital Earth, Chinese Academy of Sciences No. 2014LDE015.

The Vaihingen data set was provided by the German Society for Photogrammetry, Remote Sensing and Geo- information (DGPF) (Cramer, 2010): <http://www.ifp.uni-stuttgart.de/dgpf/DKEP-Allg.html> (in German). The authors would also like to acknowledge the provision of the Strasbourg dataset by Professor Pierre Grussenmeyer, INSA Strasbourg, Graduate School of Science and Technology.

### Author Contributions

Hongtao Wang has proposed the semantic decomposition method, implemented and conducted the tests on the data sets. Wuming Zhang proposed the primitive-based modeling method and guided the research work related to this method. Yiming Chen did research on the segmentation of the buildings and roofs. Kai Yan did research on features extraction from the aerial imagery. Mei Chen evaluated the proposed modeling method using real data set.

### Conflicts of Interest

The authors declare no conflict of interest.

### References

1. Habib, A.F.; Zhai, R.; Kim, C. Generation of complex polyhedral building models by integrating stereo-aerial imagery and LiDAR data. *Photogramm. Eng. Remote Sens.* **2010**, *76*, 609–623.
2. Haala, N.; Kada, M. An update on automatic 3D building reconstruction. *ISPRS J. Photogramm. Remote Sens.* **2010**, *65*, 570–580.

3. Rottensteiner, F.; Briese, C. Automatic generation of building models from LiDAR data and the integration of aerial images. *Int. Arch. Photogramm. Remote Sens. Spat. Inf. Sci.* **2003**, *34*, 174–180.
4. Tarsha-Kurdi, F.; Landes, T.; Grussenmeyer, P. Extended RANSAC algorithm for automatic detection of building roof planes from LiDAR data. *Photogramm. J. Finl.* **2008**, *21*, 97–109.
5. Vosselman, G.; Dijkman, S. 3D building model reconstruction from point clouds and ground plans. *Int. Arch. Photogramm. Remote Sens. Spat. Inf. Sci.* **2001**, *34*, 37–44.
6. Xiao, Y.; Wang, C.; Li, J.; Zhang, W.; Xi, X.; Wang, C.; Dong, P. Building segmentation and modeling from airborne LiDAR data. *Int. J. Digit. Earth* **2014**, *5*, 1–16.
7. Sampath, A.; Shan, J. Segmentation and reconstruction of polyhedral building roofs from aerial LiDAR point clouds. *IEEE Trans. Geosci. Remote Sens.* **2010**, *48*, 1554–1567.
8. Zhou, Q.Y.; Neumann, U. 2.5D building modeling by discovering global regularities. In Proceedings of the 2012 IEEE Conference on Computer Vision and Pattern Recognition (CVPR), Providence, RI, USA, 16–21 June 2012; pp. 326–333.
9. Dorninger, P.; Pfeifer, N. A comprehensive automated 3D approach for building extraction, reconstruction, and regularization from airborne laser scanning point clouds. *Sensors* **2008**, *8*, 7323–7343.
10. You, H.J.; Zhang, S.Q. 3D building reconstruction from aerial CCD image and sparse laser sample data. *Opt. Lasers Eng.* **2006**, *44*, 555–566.
11. Sohn, G.; Dowman, I. Data fusion of high-resolution satellite imagery and LiDAR data for automatic building extraction. *ISPRS J. Photogramm. Remote Sens.* **2007**, *62*, 43–63.
12. Seo, S. Model-Based Automatic Building Extraction from LiDAR and Aerial Imagery. Ph.D. Thesis, The Ohio State University, Columbus, OH, USA, 2003.
13. Rottensteiner, F.; Trinder, J.; Clode, S.; Kubik, K. Fusing airborne laser scanner data and aerial imagery for the automatic extraction of buildings in densely built-up areas. *Int. Arch. Photogramm. Remote Sens.* **2004**, *35*, 512–517.
14. Ma, R. Building Model Reconstruction from LiDAR Data and Aerial Photographs. Ph.D. Thesis, The Ohio State University, Columbus, OH, USA, 2004.
15. Kim, C.J.; Habib, A. Object-based integration of photogrammetric and LiDAR data for automated generation of complex polyhedral building models. *Sensors* **2009**, *9*, 5679–5701.
16. Cheng, L.A.; Gong, J.Y.; Li, M.C.; Liu, Y.X. 3D building model reconstruction from multi-view aerial imagery and LiDAR data. *Photogramm. Eng. Remote Sens.* **2011**, *77*, 125–139.
17. Chen, L.C.; Teo, T.A.; Shao, Y.C.; Lai, Y.C.; Rau, J.Y. Fusion of LiDAR data and optical imagery for building modeling. *Int. Arch. Photogramm. Remote Sens.* **2004**, *35*, 732–737.
18. Kwak, E. Automatic 3D Building Model Generation by Integrating LiDAR and Aerial Images Using a Hybrid Approach. Ph.D. Thesis, University of Calgary, Calgary, AB, Canada, 2013.
19. Awrangjeb, M.; Zhang, C.S.; Fraser, C.S. Automatic extraction of building roofs using LiDAR data and multispectral imagery. *ISPRS J. Photogramm. Remote Sens.* **2013**, *83*, 1–18.
20. Brenner, C. Constraints for modelling complex objects. *Int. Arch. Photogramm. Remote Sens. Spat. Inf. Sci.* **2005**, *36*, 49–54.

21. Brenner, C. Modelling 3D objects using weak CSG primitives. *Int. Arch. Photogramm. Remote Sens. Spat. Inf. Sci.* **2004**, *35*, 1085–1090.
22. Verma, V.; Kumar, R.; Hsu, S. 3D building detection and modeling from aerial LiDAR data. In Proceedings of the 2006 IEEE Conference on Computer Vision and Pattern Recognition(CVPR), New York, NY, USA, 17–22 June 2006; pp. 2213–2220.
23. Maas, H.G.; Vosselman, G. Two algorithms for extracting building models from raw laser altimetry data. *ISPRS J. Photogramm. Remote Sens.* **1999**, *54*, 153–163.
24. Kada, M.; McKinley, L. 3D building reconstruction from lidar based on a cell decomposition approach. *Int. Arch. Photogramm. Remote Sens. Spat. Inf. Sci.* **2009**, *38*, 47–52.
25. Henn, A.; Groger, G.; Stroh, V.; Plumer, L. Model driven reconstruction of roofs from sparse LiDAR point clouds. *ISPRS J. Photogramm. Remote Sens.* **2013**, *76*, 17–29.
26. Haala, N.; Brenner, C. Extraction of buildings and trees in urban environments. *ISPRS J. Photogramm. Remote Sens.* **1999**, *54*, 130–137.
27. Tseng, Y.H.; Wang, S.D. Semi-automated building extraction based on CSG model-image fitting. *Photogramm. Eng. Remote Sens.* **2003**, *69*, 171–180.
28. Suveg, D.; Vosselman, G. Reconstruction of 3D building models from aerial images and maps. *ISPRS J. Photogramm. Remote Sens.* **2004**, *58*, 202–224.
29. Lafarge, F.; Descombes, X.; Zerubia, J.; Pierrot-Deseilligny, M. Structural approach for building reconstruction from a single DSM. *IEEE Trans. Pattern Anal. Mach. Intell.* **2008**, *32*, 135–147.
30. Huang, H.; Brenner, C.; Sester, M. A generative statistical approach to automatic 3D building roof reconstruction from laser scanning data. *ISPRS J. Photogramm. Remote Sens.* **2013**, *79*, 29–43.
31. Vosselman, G.; Veldhuis, H. Mapping by dragging and fitting of wire-frame models. *Photogramm. Eng. Remote Sens.* **1999**, *65*, 769–776.
32. Durupt, M.; Taillandier, F. Automatic building reconstruction from a digital elevation model and cadastral data: An operational approach. *Int. Arch. Photogramm. Remote Sens. Spat. Inf. Sci.* **2006**, *36*, 142–147.
33. Wang, S.; Tseng, Y.H. Least squares model image fitting of floating models for building extraction from images. *J. Chin. Inst. Eng.* **2009**, *32*, 667–677.
34. Gruen, A.; Wang, X. Cc-modeler: A topology generator for 3D city models. *ISPRS J. Photogramm. Remote Sens.* **1998**, *53*, 286–295.
35. Wang, S.; Tseng, Y.H.; Chen, L.C. Semi-automated model-based building reconstruction by fitting models to versatile data. In Proceedings of the 29th Asian Conference on Remote Sensing, Colombo, Sri Lanka, 10–14 November 2008.
36. Haala, N.; Becker, S.; Kada, M. Cell decomposition for the generation of building models at multiple scales. *Int. Arch. Photogramm. Remote Sens. Spat. Inf. Sci.* **2006**, *36*, 19–24.
37. Oude Elberink, S.; Vosselman, G. Building reconstruction by target based graph matching on incomplete laser data: Analysis and limitations. *Sensors* **2009**, *9*, 6101–6118.
38. Lin, H.; Gao, J.Z.; Zhou, Y.; Lu, G.L.; Ye, M.; Zhang, C.X.; Liu, L.G.; Yang, R.G. Semantic decomposition and reconstruction of residential scenes from LiDAR data. *ACM Trans. Graph.* **2013**, *32*, 6601–6610.

39. Xiong, B.; Oude Elberink, S.; Vosselman, G. A graph edit dictionary for correcting errors in roof topology graphs reconstructed from point clouds. *ISPRS J. Photogramm. Remote Sens.* **2014**, *93*, 227–242.
40. Perera, G.S.N.; Maas, H.G. Cycle graph analysis for 3D roof structure modelling: Concepts and performance. *ISPRS J. Photogramm. Remote Sens.* **2014**, *93*, 213–226.
41. Zhang, W.; Wang, H.; Chen, Y.; Yan, K.; Chen, M. 3D building roof modeling by optimizing primitive's parameters using constraints from lidar data and aerial imagery. *Remote Sens.* **2014**, *6*, 8107–8133.
42. Axelsson, P. DEM generation from laser scanner data using adaptive TIN models. *Int. Arch. Photogramm. Remote Sens.* **2000**, *33*, 111–118.
43. Rusu, R.B. Semantic 3D object maps for everyday manipulation in human living environments. *Künstl. Intell.* **2010**, *24*, 345–348.
44. Chen, D.; Zhang, L.; Li, J.; Liu, R. Urban building roof segmentation from airborne LiDAR point clouds. *Int. J. Remote Sens.* **2012**, *33*, 6497–6515.
45. Edelsbrunner, H.; Kirkpatrick, D.; Seidel, R. On the shape of a set of points in the plane. *IEEE Trans. Inf. Theory* **1983**, *29*, 551–559.
46. Chaudhuri, D.; Samal, A. A simple method for fitting of bounding rectangle to closed regions. *Pattern Recognit.* **2007**, *40*, 1981–1989.
47. Canny, J. A computational approach to edge detection. *IEEE Trans. Pattern Anal. Mach. Intell.* **1986**, *8*, 679–698.
48. Fischler, M.A.; Bolles, R.C. Random sample consensus: A paradigm for model fitting with applications to image analysis and automated cartography. *Commun. ACM* **1981**, *24*, 381–395.
49. Marquardt, D.W. An algorithm for least-squares estimation of nonlinear parameters. *J. Soc. Ind. Appl. Math.* **1963**, *11*, 431–441.
50. ISPRS Test Project on Urban Classification and 3D Building Reconstruction. Available online: [http://www.itc.nl/isprs\\_wgiii4/docs/complexscenes.pdf](http://www.itc.nl/isprs_wgiii4/docs/complexscenes.pdf) (accessed on 7 August 2015).
51. Sampath, A.; Shan, J. Building boundary tracing and regularization from airborne LiDAR point clouds. *Photogramm. Eng. Remote Sens.* **2007**, *73*, 805–812.
52. Xiong, B.; Jancosek, M.; Oude Elberink, S.; Vosselman, G. Flexible building primitives for 3D building modeling. *ISPRS J. Photogramm. Remote Sens.* **2015**, *101*, 275–290.
53. Rottensteiner, F.; Sohn, G.; Gerke, M.; Wegner, J.D.; Breitkopf, U.; Jung, J. Results of the ISPRS benchmark on urban object detection and 3D building reconstruction. *ISPRS J. Photogramm. Remote Sens.* **2013**, *93*, 256–271.
54. ISPRS Test Project on Urban Classification and 3D Building Reconstruction: Results. Available online: [http://brian94.de/ISPRSIII\\_4\\_Test\\_results/tests\\_datasets\\_results\\_main.html](http://brian94.de/ISPRSIII_4_Test_results/tests_datasets_results_main.html) (accessed on 30 July 2015).
55. Rau, J.Y. A line-based 3D roof model reconstruction algorithm: TIN-merging and reshaping (TMR). In Proceedings of the ISPRS Annals of the Photogrammetry, Remote Sensing and Spatial Information Sciences, Melbourne, Australia, 25 August–1 September 2012; pp. 287–292.

56. Sohn, G.; Huang, X.F.; Tao, V. Using a binary space partitioning tree for reconstructing polyhedral building models from airborne LiDAR data. *Photogramm. Eng. Remote Sens.* **2008**, *74*, 1425–1438.
57. He, Y.; Zhang, C.; Fraser, C. A line-based spectral clustering method for efficient planar structure extraction from lidar data. In Proceedings of ISPRS Annals of the Photogrammetry, Remote Sensing and Spatial Information Sciences, Antalya, Turkey, 11–13 November 2013; pp. 103–108.

© 2015 by the authors; licensee MDPI, Basel, Switzerland. This article is an open access article distributed under the terms and conditions of the Creative Commons Attribution license (<http://creativecommons.org/licenses/by/4.0/>).